JGR Solid Earth

RESEARCH ARTICLE
10.1029/2019JB017342

Special Section:
Physical Properties of Rocks, Friction and Fracturing: The Walsh Volume

Seismo-Mechanical Response of Anisotropic Rocks Under Hydraulic Fracture Conditions: New Experimental Insights

S. Gehne[1], P. M. Benson[1], N. Koor[1], K. J. Dobson[2], M. Enfield[3], and A. Barber[4]

[1]Rock Mechanics Laboratory, School of Earth and Environmental Sciences, University of Portsmouth, Portsmouth, UK, [2]Department of Earth Sciences, Durham University, Durham, UK, [3]EPI Group, Wallingford, UK, [4]School of Engineering, London South Bank University, London, U.K.

Abstract Unconventional hydrocarbon resources found across the world are driving a renewed interest in mudrock hydraulic fracturing methods. However, given the difficulty in safely measuring the various controlling factors in a natural environment, considerable challenges remain in understanding the fracture process. To investigate, we report a new laboratory study that simulates hydraulic fracturing using a conventional triaxial apparatus. We show that fracture orientation is primarily controlled by external stress conditions and the inherent rock anisotropy and fabric are critical in governing fracture initiation, propagation, and geometry. We use anisotropic Nash Point Shale (NPS) from the early Jurassic with high elastic *P* wave anisotropy (56%) and mechanical tensile anisotropy (60%), and highly anisotropic (cemented) Crab Orchard Sandstone with *P* wave/tensile anisotropies of 12% and 14%, respectively. Initiation of tensile fracture requires 36 MPa for NPS at 1-km simulated depth and 32 MPa for Crab Orchard Sandstone, in both cases with cross-bedding favorable orientated. When unfavorably orientated, this increases to 58 MPa for NPS at 800-m simulated depth, far higher as fractures must now traverse cross-bedding. We record a swarm of acoustic emission activity, which exhibits spectral power peaks at 600 and 100 kHz suggesting primary fracture and fluid-rock resonance, respectively. The onset of the acoustic emission data precedes the dynamic instability of the fracture by 0.02 s, which scales to ~20 s for ~100-m size fractures. We conclude that a monitoring system could become not only a forecasting tool but also a means to control the fracking process to prevent avoidable seismic events.

Key Points:
- Fracture at elevated confining pressures was preceded by the maximum fluid pressure some 0.05 s earlier and accompanied by supraexponential increase in acoustic emission; this is consistent with rock type (shale and sandstone) tested
- Shale fracturing in the short-transverse mode (splitting beds) required lower fluid injection pressure (~36 MPa) and generates a simple fracture and short AE response
- Shale fracturing in the divider mode (crossing many bed simultaneously) required higher fluid pressure (~58 MPa) and is accompanied by a longer AE response and high-complex fracture geometry

Supporting Information:
- Supporting Information S1

Correspondence to:
S. Gehne and P. M. Benson,
stephan.gehne@port.ac.uk;
philip.benson@port.ac.uk

Citation:
Gehne, S., Benson, P. M., Koor, N., Dobson, K. J., Enfield, M., & Barber, A. (2019). Seismo-mechanical response of anisotropic rocks under hydraulic fracture conditions: New experimental insights. *Journal of Geophysical Research: Solid Earth*, *124*, 9562–9579. https://doi.org/10.1029/2019JB017342

Received 11 JAN 2019
Accepted 24 AUG 2019
Accepted article online 29 AUG 2019
Published online 14 SEP 2019

1. Introduction

Hydrofracturing is a common process in many areas of pure and applied geosciences, such as magma and dike intrusions (e.g., Rubin, 1993; Tuffen & Dingwell, 2005) and the development of mineral veins (e.g., Gudmundsson & Brenner, 2001). The generation of fresh tensile fracture networks by hydraulic fracturing, usually in low porosity mudrocks, has also become a key process for the exploitation of unconventional hydrocarbon resources (Montgomery & Smith, 2010). Although controversial, this practice has added significant gas resources to the U.S. market and has potential in other regions including across Europe (Andrews, 1986) where significant unconventional resources have been identified. However, environmental and public safety concerns around groundwater contamination and seismicity have frequently prevented wider exploitation (Currie et al., 2017; Howell, 2018). A key issue lies in the fact that testing strategies often rely on simple "trial-and-error" test methods in the field whose outcome cannot be easily assessed. While this approach might be adopted in formations with a relatively simple subhorizontal structure, it would represent a far riskier approach in areas with a high level of structural complexity, such as those in the United Kingdom (and in Europe generally). Here, basins are often folded and faulted on a variety of scales (e.g., Jackson & Mulholland, 1993), with those of Carboniferous age showing an especially complex structure due to an extended history of geological deformation spanning 300 million years. This complexity generates heterogeneities leading to stress localizations that are known to be important for fracture initiation and propagation (Renard et al., 2009; Scholz, 1968), with the effect of bedding planes, then significantly influencing the propagation of hydraulic fractures across different lithologies (Chitrala et al., 2010; He et al., 2016).

Due to these concerns, the monitoring of hydraulic fracturing is becoming increasingly important with the detection of microseismicity during multistage horizontal fracturing proving particularly effective as a monitoring tool (Eaton et al., 2013; Hurd & Zoback, 2012; Pearson, 1981; Warpinski et al., 2012). Several studies

have investigated the seismic characteristics of these microseismic signals and have reported the occurrence of long-period seismic events and "tremor-like" events in various reservoirs during hydrofracture (Bame & Fehler, 1980; Das & Zoback, 2013; Ferrazzini et al., 1990; Kumar et al., 2016; Mitchell et al., 2013). Non-Darcian flow and fracture resonance in wellbore-scale features have also been noted as likely sources of this diagnostic seismicity (e.g., Tary et al., 2014). Finally, similar events have been recorded in other settings, such as in volcanic and hydrothermal systems (e.g., Chouet, 1996; Chouet, 2003; Kumagai & Chouet, 2000). Here, similar seismic characteristics of long-period (or so-called "low frequency") events and tremor have long been associated with and initial high-amplitude tensile fracture event followed by subsequent fluid migration into the newly generated fracture. For both the reservoir and volcano-tectonic cases such mechanisms are entirely plausible as fluids are injected into the surrounding country rock and damage zone.

In an attempt to better understand the hydrofracture process, numerous laboratory studies investigating fluid-driven fracturing have been developed and reported (e.g., Clifton et al., 1976; Haimson & Fairhurst, 1969a; Lin et al., 2017; Li et al., 2018; Schmitt & Zoback, 1992; Stoeckhert et al., 2015; Stanchits et al., 2011, 2014; Vinciguerra et al., 2004; Zoback et al., 1977). These previous studies range from complex and costly true triaxial simulations (Li et al., 2018) to the use of effective confining triggers on critically loaded conventional samples to induce shear failure due to increasing pore fluid (Stanchits et al., 2011). While such methods allow a degree of control that is difficult in a field setting, an obvious challenge is the smaller scale of these experiments. Fortunately, a number of studies have established scaling laws between the scale of investigation and the generated fracture energy (e.g., Aki & Richards, 2013; Benson et al., 2008; Burlini et al., 2007). This is particularly true of seismic sequences that follow scale-invariant relationships and therefore allow similar statistics be used across wide range of scales (Hatton et al., 1994; Main, 2000). This is important, as a number of experiments, such as those above, have now established baseline data between fluid overpressure and tensile fracture. Despite this, the detail of the hydrostatic fluid pressure and the induced fracturing in anisotropic rocks (such as shale) remains not fully understood, although some work on fracture initiation and propagating in anisotropic media has been reported (e.g. Sesetty & Ghassemi, 2018). Importantly, the process is then also modified by factors such as the external stress conditions (such as burial depth) as well as the presence of pore pressure. These relationships are critical to develop an updated, engineered approach to hydraulic fracturing in an effort to reduce risks, increase controllability, and to optimize gas extraction but also to develop a general theory between breakdown pressure, burial depth (pressure), geological characteristics, and the tensile strength of the rock. In addition, to better employ microseismicity as a monitoring tool, adding techniques such as acoustic emission (AE; the laboratory analogs of field based seismicity) to the hydromechanical system could allow new field calibrations to be derived.

Here we address some of these challenges by simulating the generation of hydraulic fractures and relating this to rock fabric (orientation of bedding planes) simultaneously with induced seismicity (AE) and using high-speed fluid-mechanical data recording to capture the fracture process. We report a comprehensive suite of experiments with particular focus on the understanding of progressive hydraulic fracturing process and the influence of boundary conditions, which are naturally predetermined by in situ stresses and mechanical and geological properties including strength, heterogeneities, rock fabric, anisotropy, and discontinuities. To achieve this, we induce hydraulic fracturing in a conventional triaxial cell, which is combined with high-resolution recording of the mechanical data (stress and strain) and fluid pressures, geophysical monitoring provided through AE, and verified using posttest micro X-ray CT imaging. Hydraulic fracturing is a complex process, and simply evaluating the fluid pressure curve does not capture the full complexity of the fracturing process. Therefore, and unlike previous laboratory methods that have relied on the use of an inner rubber membrane to stress the inner bore of a thick walled cylinder (Vinciguerra et al., 2004), we apply direct fluid pressurization, recording mechanical and acoustic data at a high sampling rate to capture the dynamic fracture.

2. Methods: A Laboratory Procedure for Microhydraulic Fracturing

Hydraulic fracturing experiments were carried out in a triaxial deformation cell (Figure 1a) consisting of a servo-hydraulic axial and radial (confining) pressure system balanced to allow hydrostatic compensation, and a pore fluid injection pump (distilled water). A right cylindrical sample with centrally drilled conduit is prepared (see methods in the supporting information for detail) and fitted with an internal steel

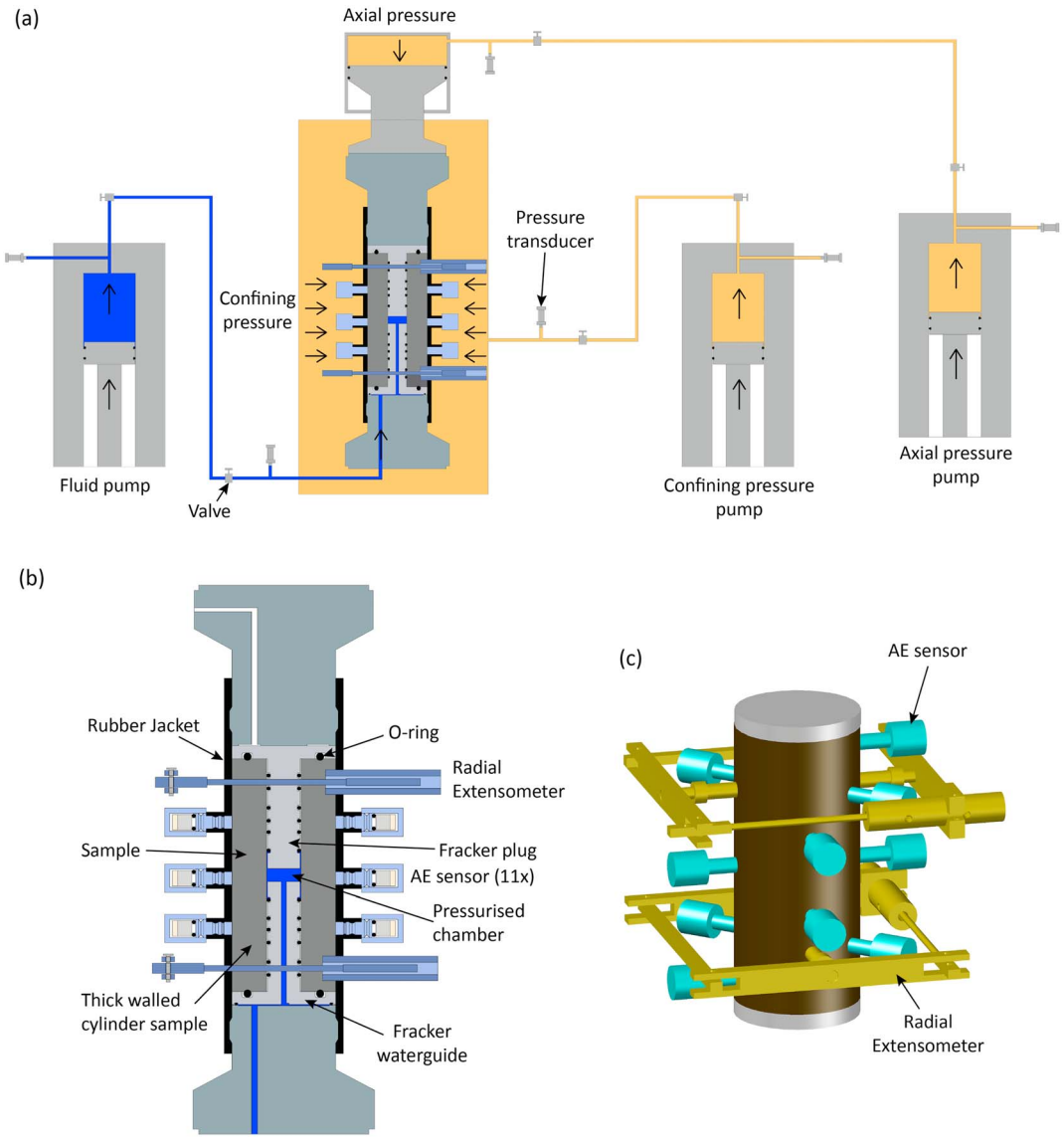

Figure 1. Hydraulic fracturing laboratory setup. (a) Schematic of the TRX apparatus setup for hydraulic fracturing experiment, (b) zoom in of sample setup, and (c) 3-D view of the sample setup with acoustic emission (AE) sensors and radial extensometers (without rubber jacket).

guide/assembly to direct pressurized fluid into a section sealed using a number of O-rings. Pore fluid is in direct contact with the sample, which is fractured in an initially dry state. This is due to the extreme difficulty in ensuring that the shale (of 10^{-20} m^2 permeability) was fluid saturated, potentially leading to confusion as to partial saturation effects and poor comparisons to the sandstone, of another level of saturation. Two experiments were attempted with "saturated" shale sample with the same pressure behavior, and similar breakdown pressure was recorded compared to the dry samples. However, as we cannot guarantee that the shale sample was fully saturated (despite 15 days of saturation), only dry data are presented. This allows tensile fractures to be initiated from the predefined zone inside the sample (Figure 1b). This allows the pore fluid to pressurize the central pressure without using a rubber lining (Stoeckhert et al., 2015; Vinciguerra et al., 2004) permitting direct evaluation between permeability, induced seismicity, and overpressure to be analyzed. To account for sample anisotropy, samples are prepared with bedding planes either parallel or normal to the major principal stress direction (σ_1).

This particular (mature) shale was selected partly for its ability to be easily prepared and machined (Forbes Inskip et al., 2018; Text S1); a selection of samples were scanned and micro-CT images taken before the

hydraulic fracturing experiment to check for preexisting fractures within the sample (Figure SF1). The entire sample assembly is separated from the confining medium using an engineered nitrile jacket fitted with ports for 11 AE sensors evenly distributed over the sample (Figure 1c; Sammonds, 1999). The AE sensors consist of a 3.5-mm-diameter disk of PZT-5A (Lead Zirconate Titanate) in compressional mode (1-MHz peak frequency sensitivity), backed by a tungsten electrode. This is sealed in an aluminum enclosure that incorporates a 12-mm waveguide fitted with a groove and notch for jacket sealing (Fazio et al., 2017). Voltages from the sensors pass though coaxial feedthroughs from the pressure vessel into dual buffered amplifiers where they are amplified by 30–70 dB (selectable) and into two independent AE recorders for simultaneous triggered and continuous AE recording (Fazio et al., 2017). Both systems record AE at 16-bit resolution and 10-MHz sampling rate, with the continuous "Richter" system used for postexperiment processing (Benson et al., 2007). In this study only the continuous system was used, with voltages amplified by 40 dB (Text S2). Two additional cantilever-type radial strain probes (Figure 1c) are attached directly to the sample at 90° to each other, with an average output calculated via $\sqrt{(r_A{}^2 + r_B{}^2)}$, where r_A and r_B are the two radial outputs, to monitor an average radial strain and crack opening displacement.

To capture the high-speed process of fluid-driven tensile failure, we employ additional transducers to measure pore fluid pressures, axial stress, and axial displacement, in addition to the standard sensors used for triaxial system feedback and control (logged at 1 sample per second, or 1 Hz). These additional transducers (as well as the radial cantilevers above) were conditioned and logged by a secondary high-speed data acquisition unit (NI-DAQ 6341) recording data at 10 kHz. To ensure accurate time synchronization, the pore fluid pressure output voltage was split between this 10-kHz system and recorded on the continuous AE recorder and thus sampled at 10 MHz. In this way the pore fluid pressure data feed is recorded simultaneously on two separate recording systems (10 kHz and 10 MHz) allowing any time offset to be calculated and applied by cross correlation, with the AE recorder acting as the "master time." Although other methods have been successfully used to investigate detailed prepeak and postpeak behavior in deforming rocks, such as via AE feedback as part of the control loop to slow the deformation rate (Lockner et al., 1991), we did not attempt this here due to the short time window that would likely have been available in a tensile fracture regime, compared to that in a compressional (shear) setup. Experiments are typically carried out in two phases.

First, an initial triaxial stress (σ_1) and confining pressure (*Pc*) are applied until the required experimental (based on a desired *Pc*) conditions are established. An initial ratio between axial stress (σ_1) to confining pressure (*Pc*) of approximately 1.25:1 was used so as to establish a "basic" triaxial condition where samples were firmly held and to prevent the initial fluid injection back-pressure from lifting the axial stress piston (the process of fluid-driven fracture necessarily require high injection fluid pressures). Second, the experiment commences (Figure S2) when water is injected at a constant flow rate (1 ml/min for shale and 5 ml/min for the sandstone to account for the higher permeability). After approximately 150 s, pore pressure increases linearly with the axial stress set to track the pore fluid pressure and exceeding it by approximately 7.5 MPa to ensure effective sealing (Figure SF2). As the full experiment is some 500 s long, and the detail of the peak and postpeak behavior spans at most 600 ms, we focus our results on the 500 ms after peak fluid injection is recorded. As expected, the developing fracture forms a link between the zones of high pressure (the overpressured conduit) to the zone of lower pressure (the radial confining pressure). Once generated, it is then likely that the fracture extends in the direction of the local maximum stress (σ_1), which is vertical in this setup, as observed posttest.

The rocks selected were Nash Point Shale (NPS) and Crab Orchard Sandstone (COS) due to their low permeability and high anisotropy; these are key characteristics of unconventional reservoirs and play a major role for the fracture behavior. NPS is part of the Porthkerry Member (Blue Lias Formation) from the Early Jurassic (190–200 ma). It is highly anisotropic (V_p anisotropy 56%; Figure SF3), with a porosity of 6.31% ± 0.75% and a very low permeability (Argon) in the nano-Darcy range. The rock consists of carbonates (≈60%), clay (≈20%), and silicates (≈20%). The rock matrix is fine grained with calcite cement and lithic fragments, predominantly quartz and chlorite. The average tensile strength (Indirect Brazilian disc method) is 4.7 MPa parallel to bedding and 8.8 MPa normal to bedding (Figure SF4). COS is a fine grained, cross-bedded fluvial sandstone with a very low permeability in the micro-Darcy range (Argon) and a porosity of 7.1% ± 0.2%. The rock is anisotropic (V_p anisotropy 13%; Figure SF3) and consists predominantly of quartz (>85%) with minor contents of feldspar and lithics and is cemented by sericitic clay (Atkinson, 1979;

Gehne & Benson, 2017). Grains are approximately 0.25 mm in size and generally without a preferred alignment. The average tensile strength (Indirect Brazilian disc method) parallel to bedding is 8.6 and 9.8 MPa normal to bedding (Figure SF4). Further data may be found in Table ST1.

3. Results: Microhydraulic Fracturing of Shale and Sandstone

Data from the fluid-driven fracture process was synchronized across three separate systems taking measurements of fluid injection pressure, AE activity, and radial deformation measurements. Specifically, five key parameters are defined: (1) the maximum fluid injection pressure (**maxP$_{inj}$**); (2) the time (onset) of radial deformation (**rDef**); (3) the time (onset) of AE activity, which itself is defined as the exponential increase in AE hit count rate (**AE$_0$**; Boone et al., 1991; Martin & Chandler, 1994; Zoback et al., 1977); (4) the time of peak AE activity (**maxAE**); and finally, (5) the time at which the fluid pressure starts to decrease rapidly (**P$_{rd}$**).

Unstable crack propagation leading to sample failure (a crack connecting the inner bore to the outside radius) is denoted by a maximum or spike in the AE activity and is accompanied by a significant change in fluid pressure decay rate (Detournay & Carbonell, 1997; Rummel & Hansen, 1989). Laboratory data for NPS fracture (bedding parallel to the sample axis) at a confining pressure of 25.4 MPa is shown in Figure 2. A maximum fluid pressure of 36.3 MPa (Figure 2a) was recorded; this was used to define a time "zero" for the experiment. Shortly afterward (0.045 s), a sharp decrease in pressure injection is recorded accompanied by both a rapid increase in radial deformation and a rapid increase in AE hit rate. By integrating the P_{inj} data, the rate of pressure change becomes evident (Figure 2b), following four key stages. An initial gentle increase (0–0.04 s) is followed by a time zone of increased pressure change (0.04–0.053 s) at a maximum of approximately 50 MPa/s. Fluid pressure then enters the third (main) phase of rapid pressure decrease at 0.053 s with a maximum decay rate of 1,000 MPa/s. This significant pressure decrease to 30.3 MPa coincides with the first AE peak activity, and the continuous AE signal (Figure 2c) exhibits a sharp event at that time. The fluid pressure exhibits a single oscillation and recovers to 32.5 MPa (at 0.065 s) before finally entering a period of gradual pressure decay after 0.07 s, where pressure decay restabilizes at approximately 55 MPa/s, suggesting constant fluid pressure leakage through a fracture that cannot be maintained by the constant (controlled) fluid injection rate used.

The initial surge in AE activity is of a high amplitude pulse (Figure 2c), which quickly reaches 0.6 volts and a hit count (AE rate) of 400 events per second. The signal remains at a high level in terms of hit rate during the subsequent rebound in fluid pressure, after a short time offset (Figure 2c), but at a lower amplitude of 0.1 volts that then subsequently tapers off. Each change in fluid pressure decay rate was associated with a slight change in the radial deformation curve, which finally stabilized at 46 μm. The spectrogram (Figure 2d) shows the frequency-power components of the waveform over time, revealing an emergent onset with initial frequency up to 400/600 kHz, followed by a quasi-continuous harmonic coda with significant power at the 100 kHz. These frequencies have previously been associated with fluid movement or hybrid rock/fluid flow (Benson et al., 2008), which is clearly supported by the experimental protocol in this case. By a time index of 0.3 s, the amplitude of these signals has faded and approach background noise. The higher-frequency (400–600 kHz) events initially recorded are often associated with fresh fracture events (Benson et al., 2007) and are again supported by the experimental protocol, as they are recorded at the onset of unstable fracture propagation and fade out by a time index of approximately 0.15 s.

Figure 3 shows hydraulic fracturing data at 20.3-MPa confining pressure with the central conduit orientated normal to σ_v, forcing radial fractures to cross-bedding planes. Some mechanical characteristics of the fracture process are similar to the previous example: a rapid fluid pressure decay indicated by a peak AE rate and P_{inj} decay rate, followed by a fluid oscillation. However, a significantly higher fluid pressure is now required to initiate the fracture (58 MPa) compared to parallel to bedding (Figure 2). Some subtleties during tensile fracture formation may also be discerned. The initial decrease in fluid pressure is associated with a first phase of increased seismic activity commencing at 0.01 s (Figure 3a), which shows the main power distribution in a low-frequency range 50–200 kHz (Figure 3d). A second AE swarm starts soon after at 0.025 s and increases exponentially. Peak AE activity coincides with the increase in pressure decay rate (Figure 3b) and an increase in radial deformation rate at 0.032 s. During the rapid fluid pressure decay, pressure decay rates increase to a maximum of 7,292 MPa/s. The continuous AE waveform (Figure 3c) indicates a fast

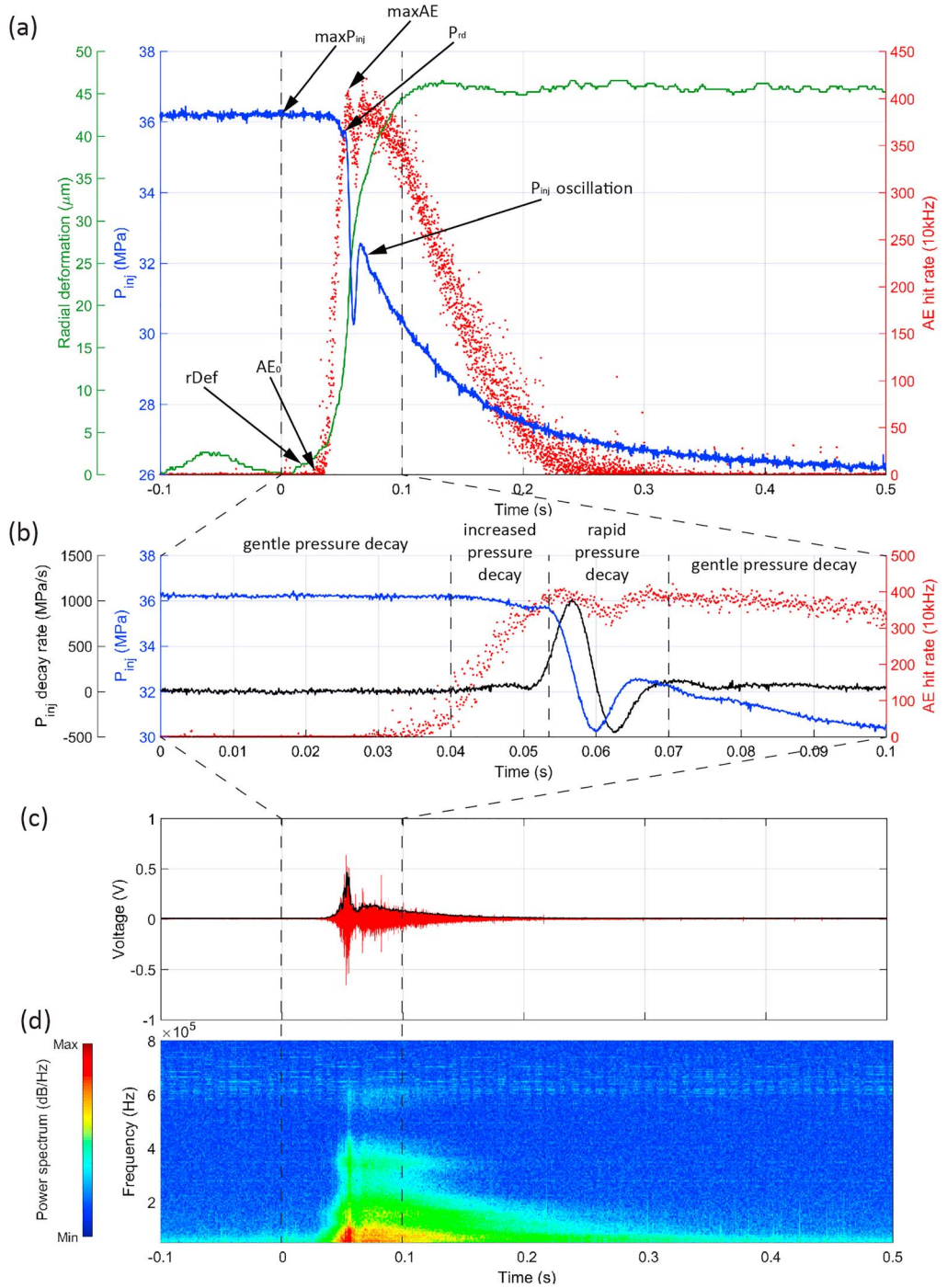

Figure 2. Laboratory data from hydraulic fracturing simulation using on Nash Point Shale at 25.4-MPa confining pressure and with bedding parallel to sample axis. (a) Time record of internal fluid injection pressure (blue line), radial deformation (green line), and acoustic emission (AE) hit counts (red dots). (b) Fluid pressure decay rate (black line), fluid pressure (blue line), and AE hit count rate (red dots). (c) Snapshot of the continuous waveform (red line) including the signal envelope at the time of failure. (d) Respective spectrogram at the time of failure. The spectrogram data illustrates the frequency range exhibiting power (color) with time. Time scales zeroed at maximum fluid injection pressure; note that due to the zoom of the time axis (just 0.6 s is shown), the pore fluid appears almost linear compared to the full experiment (e.g., Figure SF2).

emergent to impulsive onset with a sharp peak event and three frequency components; the most significant power lies in the range 50–200 kHz, and two higher-frequency components occur at 400 and 600 kHz (Figure 3d). As per the previous example, a single P_{inj} oscillation is recorded after the rapid pressure

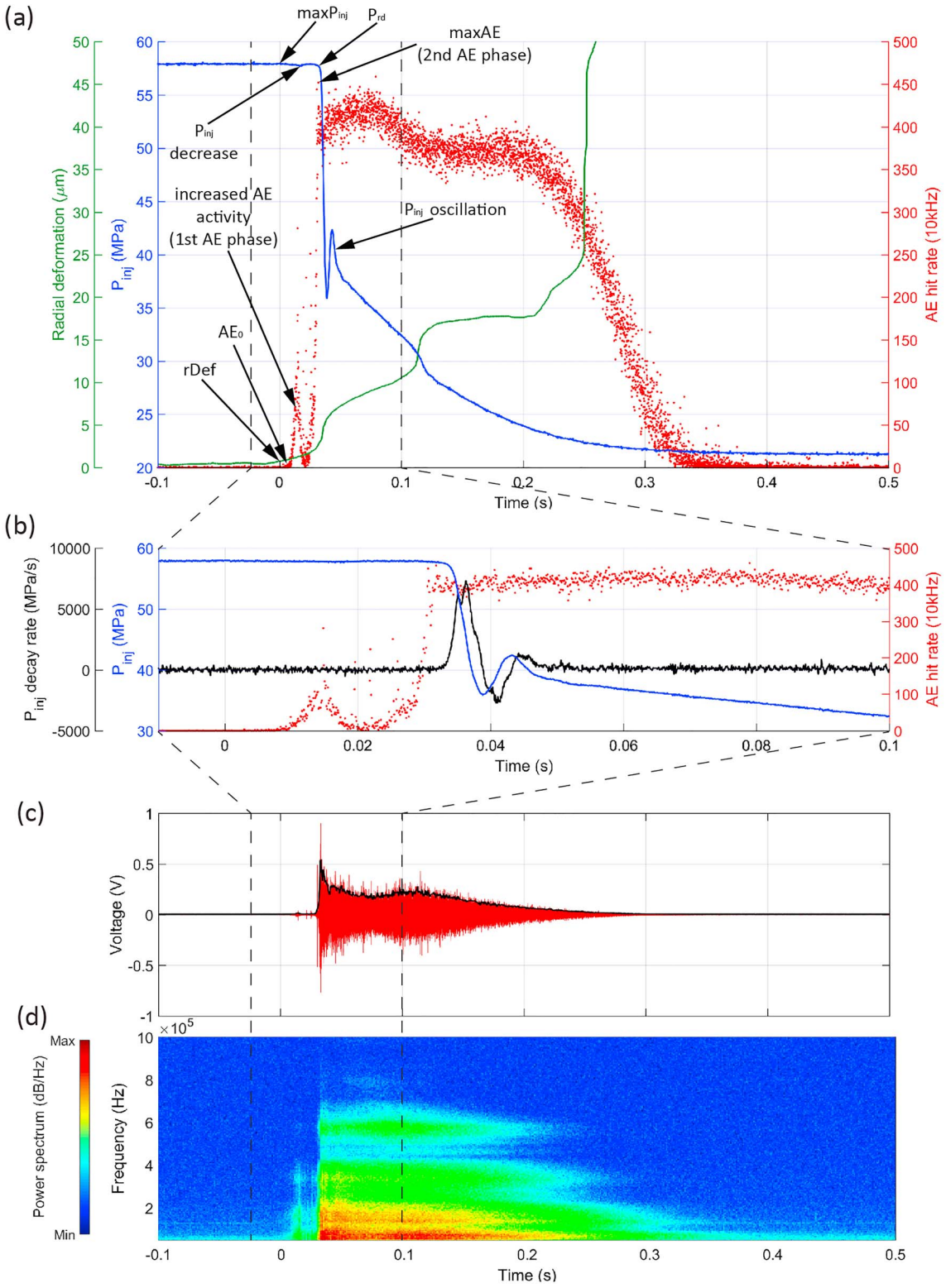

Figure 3. Laboratory data from hydraulic fracturing simulation on Nash Point Shale at 20.3-MPa confining pressure and with bedding normal to sample axis. (a) Time record of internal fluid injection pressure (blue line), radial deformation (green line), and acoustic emission (AE) hit counts (red dots). (b) Fluid pressure decay rate (black line), fluid pressure (blue line), and AE hit count rate (red dots). (c) Snapshot of the continuous waveform (red line) including the signal envelope at the time of failure. (d) Respective spectrogram at the time of failure. The spectrogram data illustrate the frequency range exhibiting power (color) with time. Time scales zeroed at maximum fluid injection pressure.

decay (Figure 3a), rebounding to 42.5 MPa. At approximately 0.12 s, a change in the fluid pressure curve coincides with a sharp increase in radial deformation and a halt in AE hit rate decrease. The following plateau in the AE rate matches the plateau in the radial deformation curve, both lasting from approximately 0.13 to 0.21 s. AE activity decreases rapidly from this point (at 0.21 s), and radial deformation increases significantly (at 0.21 and 0.025 s), indicating the end of the experiment. The AE waveform (Figure 3c) contains three frequency components that gradually fade in amplitude with higher-frequency components first at 0.2 s (600 kHz) and 0.25 s (400 kHz) compared to the low-frequency events, which last until 0.35 s (Figure 3d).

For the COS a maximum fluid injection pressure of 32.2 MPa was needed for tensile fracture with the conduit drilled parallel to bedding and using 14.4-MPa confining pressure (Figure 4). Unlike the shale data, no obvious tensile strength anisotropy was evident, with the equivalent maximum fluid pressure at failure in samples drilled normal to bedding of 29.3 MPa (Figures SF5 and SF6) consistent with ambient pressure tensile data (Figure SF4). In addition, no fluid pressure oscillations are recorded (unlike NPS data), and the onset of radial deformation and the onset of increased AE activity occur simultaneously with maxP_{inj} at 0s (Figure 4a). This is followed by a period of 0.05 s where P_{inj} gradually decreases, radial deformation gradually increases, and AE hit rate increases exponentially with significantly more hits that recorded from the NPS data sets and with the AE waveform showing a low-frequency (100–150 kHz) emergent onset (Figure 4d). At 0.05 s, AE activity peaks (Figure 4a) and fluid pressure decay rate increase to a maximum of 93 MPa/s (Figure 4b). During the main fracturing event, the continuous signal (Figure 4c) exhibits multiple peaks with energy contained between two bands of 100–300 kHz and 400–450 kHz (Figure 4d). Finally, after 0.1 s, fluid pressure decay enters a smooth decrease, and radial deformation reaches a plateau just under 7 μm (Figure 4a). During this time, AE rate also stabilizes at a level of 95 khits per second with higher-frequency events (400–450 kHz) rapidly dying out to leave a pervasive low-frequency (100–250 kHz) component (Figure 4d). At 0.195 s, radial deformation finally accelerates to sample failure signifying the end of the experiment (Figure 4a).

3.1. Hydraulic Fracture Morphology

The morphology of the fractures was derived using X-ray computed microtomography (see the supporting information for acquisition and processing protocols). For both shale and sandstone, fractures form axially and independent of bedding orientation (Figure SF7). However, for NPS samples with bedding orientated parallel to the sample axis, the developed fracture plane is planar and orientated parallel (and often along) the inherent bedding. Fractures are best described as "simple" with a homogenous fracture geometry and mainly restricted to one plane, and little bifurcation (Figure 5). The fracture aperture ranges from 20 to 60 μm and is relative uniform along the radial fracture path from the conduit to the edge of the sample. Figure 5b shows detail across three cross sections c 1 through c 3 spanning the central section of the sample fractured at 25.4 MPa, parallel to bedding. The simple tensile fracture shows little obvious "tortuosity" and largely follows the natural subbedding of the finely laminated shale.

Conversely, for NPS samples with bedding orientated normal to the sample axis (parallel bedding), fractures also propagate in the radial direction (i.e., from the inner bore of the axially drilled conduit to the edge of the sample) but with a very different character. In this case (Figure 6), the tensile fracture must now cross several bedding plans in the arrester orientation (Figure SF4), which requires more energy for fracture propagation. In addition, the fracture planes are complex and are highly bifurcated. Moving from the top of the sample, Slice 1 shows two relatively simple fracture, which then become progressively more complex in Slices 2 and 3, which straddle the main pressurized zone of the sample conduit. Here, many tensile fractures from conduit to sample edge are clearly seen (Figure 6, Zooms 1 and 2, respectively). Further down the sample, Figure 6, Slice 4, once again shows a simpler two-fracture system.

In contrast to the fine-grained matrix of the shale, the characteristics of hydrofractures in the coarser-grained sandstone are not dependent on bedding orientation, consistent with both the maximum strength at maximum injection pressure (Figures 4 and SF6) and indirect tensile strength. All micro-CT scanned sandstone samples, independent of confining pressure and bedding orientation, show a single major fracture (e.g., Figure 7) with similar fracture morphologies and damage zones extending over about half of the sample length, not reaching either the top or bottom of the sample. The geometry of the fractures are significantly influenced by the microstructure of the rock, with both intergranular (between grains—fracture grows along the grain boundaries) as well as transgranular (through grains) features seen. Intergranular crack

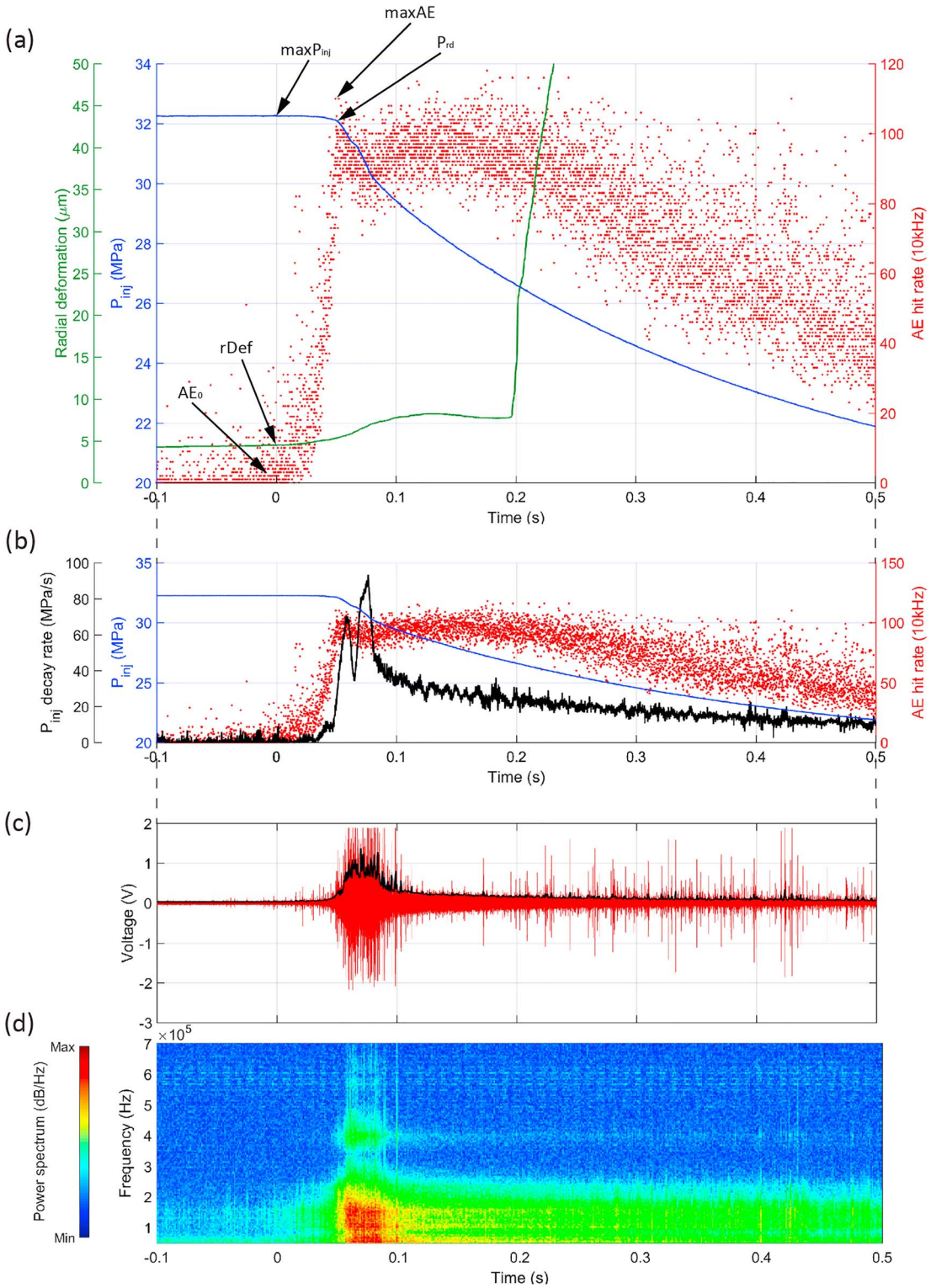

Figure 4. Laboratory data from hydraulic fracturing simulation on Crab Orchard Sandstone at 14.4-MPa confining pressure and with bedding parallel to sample axis. (a) Time record of internal fluid injection pressure (blue line), radial deformation (green line), and acoustic emission (AE) hit counts (red dots). (b) Fluid pressure decay rate (black line), fluid pressure (blue line), and AE hit count rate (red dots). (c) Snapshot of the continuous waveform (red line) including the signal envelope at the time of failure. (d) Respective spectrogram at the time of failure. The spectrogram data illustrates the frequency range exhibiting power (color) with time. Time scales zeroed at maximum fluid injection pressure.

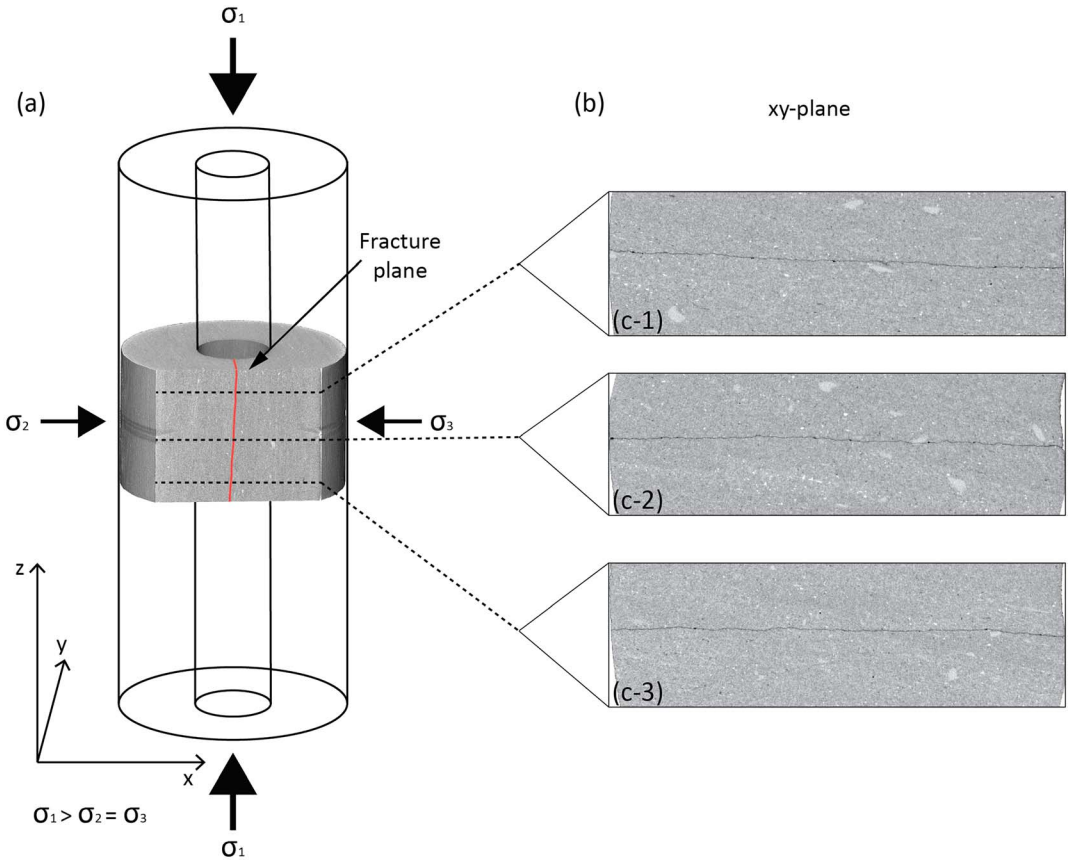

Figure 5. Fracture geometry in Nash Point Shale parallel to bedding at 25.4-MPa confining pressure (not to scale). (a) Orientation of final fracture plane (red) relative to sample geometry and imposed stress field, (b) three example cross-sectional slice c 1 to c 3 across the central pressurized zone show very little change in the character of the fractures, which are simple planar structures.

propagation is likely related to grain-bond strength (cementation) and develops a diffuse fracture geometry that strays significantly from a straight plane with high visual tortuosity evident. The high-resolution images also show that fractures in the sandstone connecting preexisting pores along the fracture path. This gives the fracture a more complex morphology than seen for the much finer shale. Using X-ray computed microtomography, aperture varies between 20 and 70 μm and becomes thinner toward the edge of the sample. Microscale kinks, bends, fracture branching, sharp diversions, and arrested fracture ends are visible along the fracture path.

4. Discussion: Understanding Hydraulic Fracturing

In general, hydraulic fracturing generates tensile fractures via a complex crack tip process zone that includes zones of cohesion and high shear stresses (e.g., De Pater, 2015). To achieve this, fluids must be injected into a rock mass (whether magma injection in volcanic settings or veining in tectonically active regions) at a rate sufficient to generate overpressure that exceeds the tensile strength of the country rock. In an engineered environment the fracture then extends by continuing to pump fluid into a conduit. This general setup applies equally as described in laboratory studies (this work) or as seen in field approaches (e.g., Gandossi, 2013; Haimson & Fairhurst, 1969b; Zoback et al., 1977). To better understand fracture networks produced by hydraulic fracture (regardless of source), it is essential to understand the rock geomechanics and the interaction of hydraulic fractures with respect to the local anisotropy and the delay between fluid pressure (which is easy to record and monitor) and the onset of fracturing (which is not). Both NPS and COS exhibit a significant time delay between maximum fluid injection pressure, fracture initiation, and the physical breakdown of the sample. A good proxy for fracture initiation is the onset of AE hit rate (e.g., Zoback et al., 1977). In all the experiments reported in this study, both the peak AE rate and rapid decay of fluid pressure were good

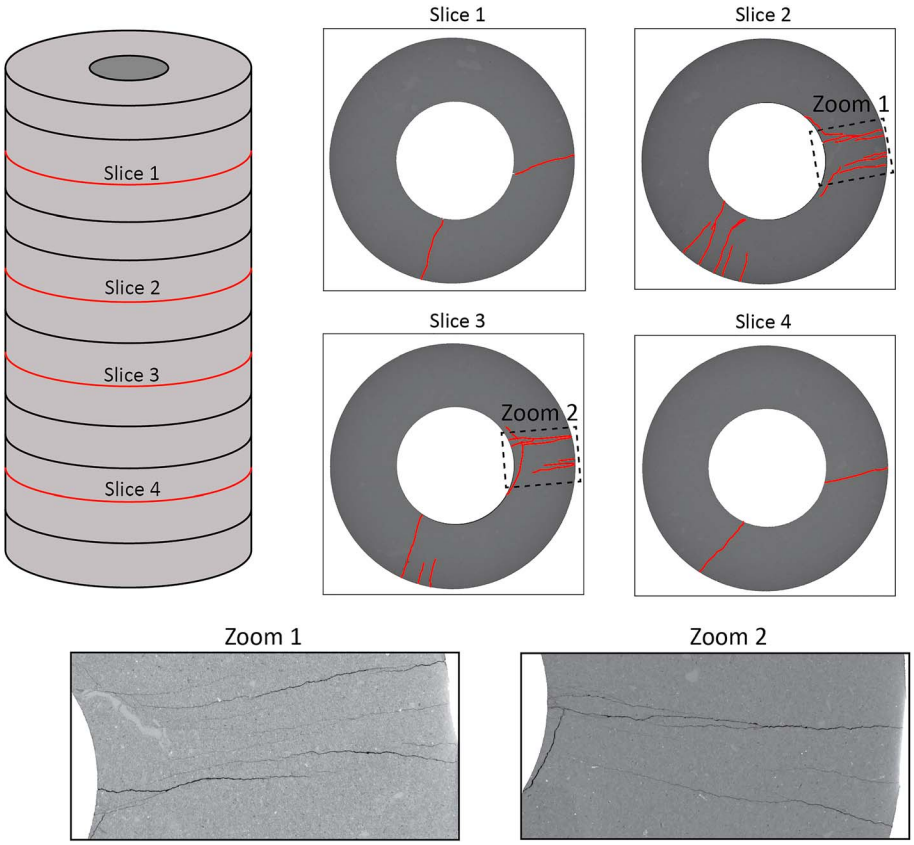

Figure 6. Fracture geometry in Nash Point Shale normal to bedding at 20.3-MPa confining pressure (illustrative for comparison to Figure 6; not to scale). Four slices (1–4) are labeled with the position on the schematic sample on the left with two zooms (1) and (2) taken from X-ray computed microtomography data.

indicators for the physical breakdown (tensile fracture initiation) of the sample. These data are further supported by radial deformation, which increases significantly at approximately the same time. To fully analyze the progressive failure during hydraulic fracturing, we have focused on three stages of the fracturing process: (1) maximum fluid injection pressure, or the maximum pressure recorded during the pressurization; (2) fracture initiation pressure, where a small initial defect develops; and (3) breakdown/failure pressure, where the sample physically fails.

By virtue of the setup used, for samples with bedding parallel to the central conduit, the developed hydraulic fractures must propagate in either the short-transverse or divider orientations. Due to the preferential weakness of the bedding planes of NPS, in the experiments the mode favored was exclusively the short-transverse

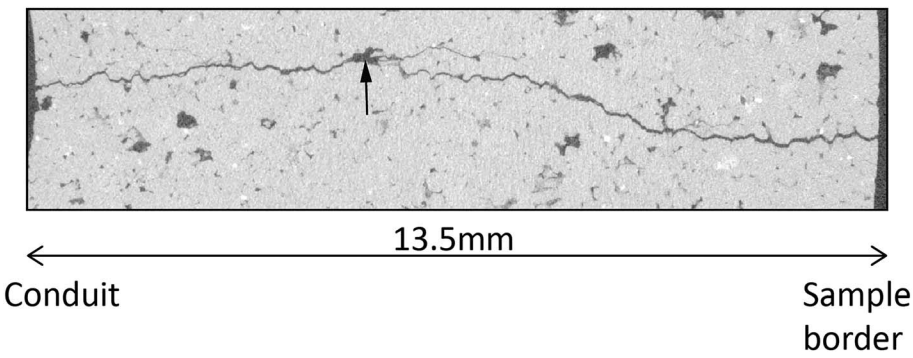

Figure 7. High-resolution images showing the fracture geometry in Crab Orchard Sandstone; black arrow indicates preexisting pore spaces.

type. For samples with bedding planes orientated parallel to the pressurizing conduit the vertically orientated fractures are forced to propagate in the Arrester orientation. In both scenarios, fractures initiate in the pressurized, central, part of the sample and propagate radially and axially. The hydromechanical characteristics of the fracture process are similar for both normal and parallel bedding: a rapid fluid pressure decay, indicated by maximum AE rate and change in fluid pressure decay rate, followed by a brief rebound/oscillation phase. However, a significantly higher fluid pressure is required to initiate hydraulic fracture normal to bedding. Fracture initiation depends on the strength of the rock material rather than the strength of the bond between bedding planes, and a material with fewer inherent flaws would likely require higher fluid pressures to initiate fracture. In addition, samples orientated with their conduit normal to bedding showed a plateau in the radial deformation. This suggests that after the initial fracture generation a change in fracture propagation occurs from radial to axial: first, the fracture propagates dominantly radially by following the shortest stress path, then, once the radial fracture reaches the edge of the sample, continuing vertically. This would infer that the fracture mode changes from propagating in the divider orientation to the arrester orientation.

All shale experiments, independent of bedding orientation or confining pressure, showed similar mechanical characteristics in terms of the initial fracture process and followed the same fracturing sequence. In general, the maximum fluid injection pressure is seen to predate fracture initiation, which is followed by an almost instantaneous pressure drop associated with unstable fracture propagation. After an initial pressure decrease, an oscillation/rebound in fluid pressure is observed before fluid pressure decreases to the level of the confining pressure (the fracture having formed a pathway for exit). Although it is not clear what causes this oscillation, a current working hypothesis is that it is caused by the fracture tip locally outpacing the driving fluid, which then catches up to further extend the crack a short time later. This is an area of further study and will be the subject of a future paper. The time delay between maximum fluid injection pressure and fracture initiation suggests an elastic or plastic behavior of the shale, a hypothesis supported by the relatively gradual change in radial deformation at the time of maximum fluid injection pressure. A similar response in thin-walled granite cylinders was observed by Schmitt and Zoback (1989), who reported an increasing compliance with increasing fluid injection pressure prior to failure, which they attributed to dilatant effects, resulting in a nonlinear strain response of the sample prior to failure. Dilatancy prior to fracture initiation has also been suggested to result in an increased permeability of the plastic deformation zone near the conduit wall (Schmitt & Zoback, 1993). This is important, as increased permeability is likely to induce compressive stresses due to the fluid infiltration acting to delay further fracturing in a negative feedback loop (Li et al., 2016).

The time period from fracture initiation to sample breakdown is most likely characterized by a stable crack propagation, as little or insufficient fluid pressure is available along the fracture surfaces to initiate unstable fracture. However, the decreasing fluid injection pressure combined with the observation of low-frequency seismic activity (e.g., Figures 2a and 2d) suggests that fluid flow does occur along the fracture, which is known to generate fluid turbulence resulting in AE (e.g., Fazio et al., 2017). This is accompanied by fracture opening that in turn allows for an almost instantaneous release of fluid pressure. Evidence for this final phase of unstable fracture propagation may be derived from the high-pressure decay rates (1,012 MPa/s for NPS samples parallel to bedding and 7,292 MPa/s for NPS samples normal to bedding), which, according to Bernoulli's principle, are proportional to fluid flow. This suggests a critical fracture velocity, crack length and energy release is exceeded and promotes unstable fracture propagation. In addition, it is likely that the time delay between fracture initiation and sample failure is linked to the time taken for the pressure to build up within the fracture, and in turn to reach the critical energy release for the transition from stable to unstable fracture propagation. It therefore follows that this delay may then be used to infer the developing fracture geometry and complexity of the tensile fracture network, useful information if more complex geometries were linked to enhanced resource exploitation.

After unstable fracture propagation, shale experiments show a recovery or oscillation in both fluid injection pressure and AE hit rate (with a small time offset), and with both following an increasing (but stepwise) radial deformation. For shale experiment, fluid oscillation suggests an incremental crack growth with the subsequent pressure peak representing the pressure to restart crack propagation. Unstable fracture propagation in the shale reflects the scenario whereby fluid demand within the fracture is higher than fluid supply (e.g., Detournay & Carbonell, 1997; Rummel & Hansen, 1989; Whittaker et al., 1992), resulting in a fluid

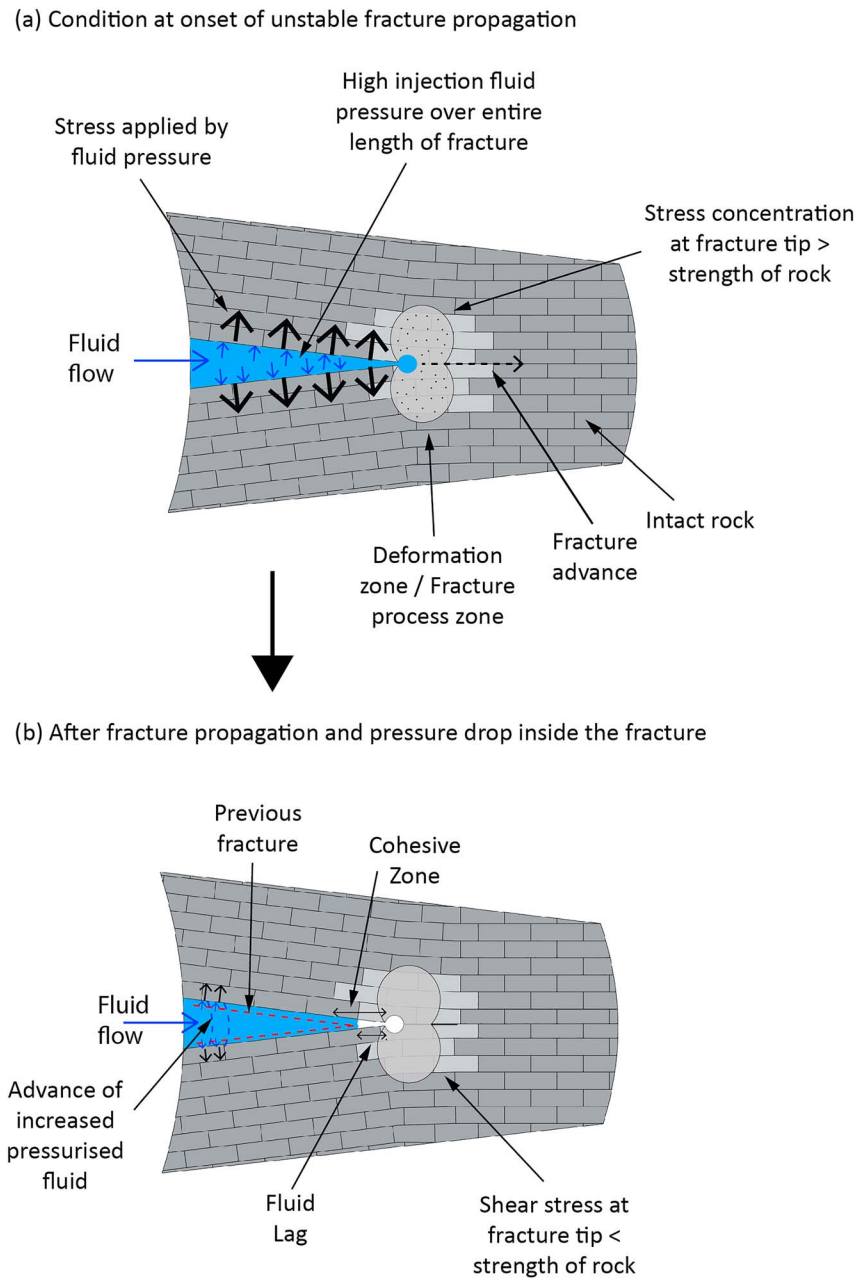

Figure 8. Conceptual model of incremental fracture propagation during hydraulic fracturing experiments with Nash Point Shale. (a) Sufficient fluid pressure has built up along the entire length of the sample (blue arrows indicate fluid pressure, and black arrows indicate stress applied on fracture walls) to generate the required stress at the fracture tip (large red ellipse at fracture tip) for unstable fracture propagation to occur with the result of fracture advance (dashed black arrow), (b) which increases the fracture volume and leads to a pressure drop inside the fracture (low-pressure zone) as fluid flow cannot maintain the pressure, reducing the stress at the fracture tip and ultimately bringing the fracture advance to a temporary halt. Fluid inflow continues, and pressure inside the fracture starts to build up again until condition (a) is reached. This cycle occurs multiple times during hydraulic fracturing experiments with Nash Point Shale.

pressure decrease. A conceptual model of the incremental fracture propagation is shown graphically in Figure 8. Initially, fluid provides sufficient stress to generate and open a Mode 1 crack (Figure 8a), which is accompanied by rising AE activity as shown in the experiments. The trend in radial deformation further agrees with the concept, with initially only a small radial deformation initially recorded. However, once the crack is opened, stress (fluid pressure) is rapidly relieved by a propagating fracture moving too fast for the fluid to replenish it (Figure 8b), resulting in the sharp decrease in fluid pressure recorded and

a cessation in AE rate. This sketch also illustrates the "kidney"-shaped process zone that absorbs stress and shields the fracture tip (Warpinski et al., 2012; Zang et al., 2019), and how the fluid lag and so-called cohesive zone may contribute to the crack tip complexity when fluids are involved (De Pater, 2015). Finally, when the fracture reaches the outer edge of the sample, fluid pressure dissipates in a steady manner (essentially, a throughgoing "leak" at this point) until it reaches confining pressure. During this phase, increased AE hit rate is recorded, likely to be related to the fracture extension in a vertical sense as shown by postexperiment analyses. Another source for the elevated AE hit rate is the fast (turbulent) fluid flow through the fracture as local pockets of turbulence generate rock-fluid coupling resulting in AE events.

Although a large number of laboratory scale experiments have been reported, including on anisotropic rocks such as shale (e.g., Li et al., 2018; Lin et al., 2017; Schmitt & Zoback, 1992), the challenge of scaling these results to field scenarios remains ever present. A common tool with which to attempt scaling is via seismicity, such as reported in mining environments (e.g., Collins et al., 2002) and volcanotectonics (e.g., Benson et al., 2010; Harrington & Benson, 2011). The seismicity generated during magmatic and/or hydrothermal fluid injection beneath volcanoes is particulary diverse, ranging from sequences due to pure fracture (e.g., Chouet, 2003) to rock/fluid interactions that often yield a lower and characteristic frequency content indicative of fluid migration (Chouet, 1996; Kumagai & Chouet, 2000). Importantly, as the statistics governing frequency-magnitude distributions are similar across a wide range of magnitudes (Hatton et al., 1994; Main, 2000), seismic sequences have been used to develop a simple scaling method (Aki & Richards, 2013; Benson et al., 2008; Burlini et al., 2007). The approach indicates that the ratio of the frequency of the recorded waveform to the size of the source is similar in both field and laboratory settings, thus providing some confidence that laboratory studies can be used to simulate field-scale processes in a holistic manner. Such comparisons can also be made using waveform data from fracking operations in the Barnett field, USA, (Das & Zoback, 2013); Fenton Hill, New Mexico (Bame & Fehler, 1980; Ferrazzini et al., 1990); and at Motney, B.C., Canada (Eaton et al., 2013), which show a qualitatively similar seismic signature to AE data generated from experiments. This is important, as reducing fluid injection-related seismicity is becoming an important goal for safe resource extraction (Zang et al., 2019).

For experiments using NPS with the conduit parallel to bedding, the orientation of the new fractures, and therefore of any new and/or enhanced permeability, is generally controlled by the orientation of the bedding planes, which likely provide planes of weakness. Posttest examination and micro-CT analysis confirm that most of the specimens fail by axial splitting, in doing so they generate a largely planar axial fracture parallel or subparallel to bedding planes (the short-transverse orientation). However, micro-CT data also suggest a likely relationship between ductility and the rock fabric, particularly the bedding planes. This is built into the graphical model in Figure 8 as rigid "sheets" or "blocks" glued together with a ductile material allowing the sheets to move apart elastically, and consistent with the mechanical (radial deformation) data. This means that fractures developing parallel to the inherent bedding rely dominantly on the strength of the bedding and follow these planes of weakness, only diverting when encountering lithic fragments (Figure 9). The reduced tensile strength due to elastic deformation in the deformation zone (e.g., Figure 9b) is likely to promote further fracture advance along the bedding plane. Hydraulic fractures propagating across the bedding planes in the arrester mode had more tortuosity and a more complex character. Fractures propagating in this mode typically interact with bedding planes to drive shear displacement on these planes (Rutter & Mecklenburgh, 2017) and result in a more tortuous fracture path. These observations suggest that the orientation of bedding planes have an influence on the developed fracture network and fracture geometry.

Conversely, experiments using COS illustrate the effect of a different rock fabric in terms of grain size and matrix, as well as the influence of initial permeability and how "ductile" the overall fabric is to pressurization. This is despite the fact that this rock has a similar porosity, and an inherent anisotropy. Despite a much higher tensile strength of the sandstone (8.6 MPa compared to 4.7 MPa for NPS), hydraulic fractures initiate at similar pressure compared to NPS but, unlike the shale, are not significantly affected by bedding orientation (17.9 MPa parallel and 13.9 MPa normal to bedding). This is likely a function of the cement bonding between the larger grains of the COS, which act as the key weakness regardless of loading direction. During our microhydraulic fracture experiments, COS revealed relatively low breakdown pressures due to this reduced tensile strength of the rock and further promoted via a combination of deformation and built-up pore pressure ahead of the fracture due to its higher intrinsic permeability (Figure 9). Depending on the baseline (prefracture) permeability, pore pressure is built up faster and over a more extensive area

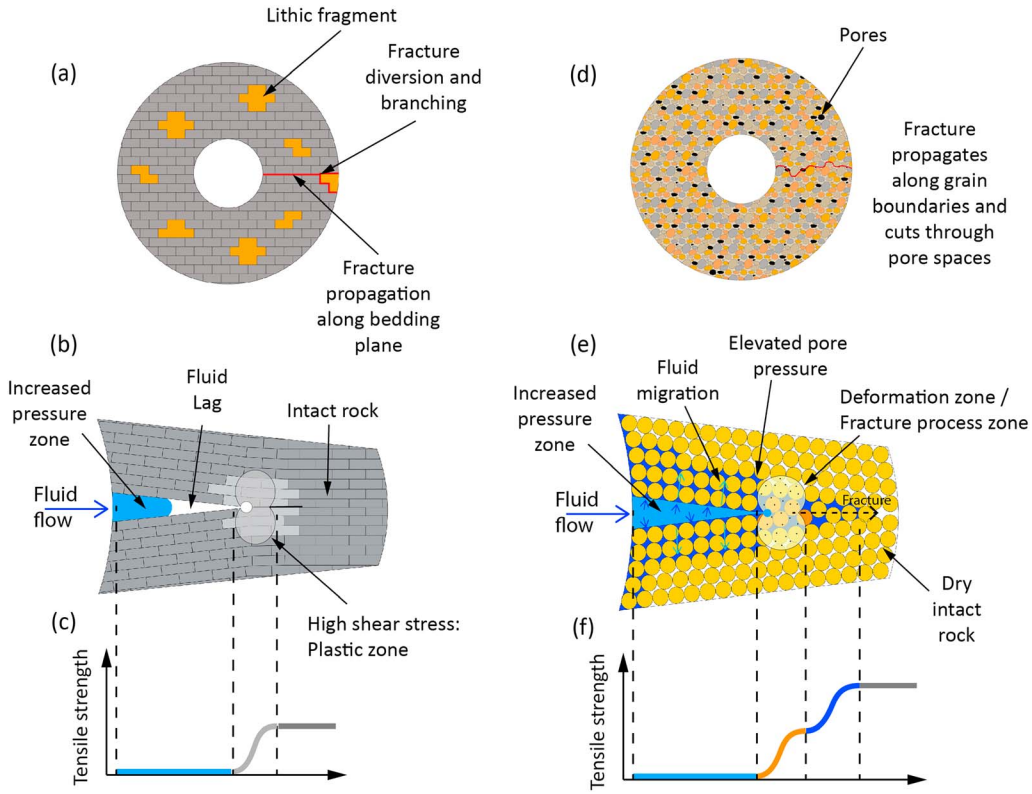

Figure 9. Conceptual model showing the interaction of rock fabric and inherent bedding planes on the fracture path and fracture network. (a) NPSx, fracture develops along bedding plane but diverts or bifurcates when encountering lithic fragments in the path; (b) NPSx, schematic diagram of an hydraulic fracture induced tensile fracture propagation showing no pressure and deformation zone; (c) NPSx, tensile strength; (d) COSx, fracture path depending on rock fabric, developing along grain boundaries and through cement; (e) COSx, schematic diagram of an HF-induced tensile fracture propagation showing zone of increased pore pressure due to fluid migration along permeability; and (f) COSx, tensile strength.

ahead of the fracture in COS, resulting in lower fracture initiation pressures. The subangular quartz grains of the COS provides a different fracture dynamic than seen in NPS, specifically longer delays between fracture initiation and sample breakdown that indicate a prolonged subcritical and stable crack development prior to unstable fracture propagation. Afterward, the connecting of preexisting pores along the fracture path in the sandstone effectively enlarges the fracture aperture (Zoback et al., 1977) allowing for the pore fluid supply to keep up with the fluid demand in the fracture. This results in a much smaller pressure decrease compared to NPS, promoting fracture propagation to the edge of the sample without the oscillatory behavior seen in the NPS where fracture outpaced the fluid. Other potential sources for the observed the oscillations, such as fluid injection rate, were discounted during the initial development of the experimental protocol. The timing of oscillation, at the precise moment of failure, also suggests a direct causal link to the new fracture pathway.

These features and ideas are summarized in Figure 9 (d–f) in which it is postulated that the fracture pathway in COS is significantly influenced by the rock fabric and discontinuities (Figure 9d). Here, induced fractures take the path of least resistance along grain boundaries and through preexisting pores and are less affected by bedding planes and their orientation. This is likely also due to the cementation in the sandstone, which is not present in the shale. The higher tortuosity of hydrofractures in the sandstone results from the correlation of grains and preexisting pores in the sandstone. It is likely that these heterogeneities modify the stress field near the crack tip and affect the propagation direction, forcing the fracture to divert and develop a diffuse fracture geometry that strays significantly from a straight plane. These observations suggest that hydraulic fracturing in COS is initially controlled by the rock permeability but then switches over to being controlled at a microscale by grain-bond strength and grain-cement boundaries (Figures 9e and 9f). However, at the

macroscale the bedding planes still influence the overall propagation direction of the fracture as they tended to propagate parallel to the bedding (with deviations). Additionally, the COS experiments showed that the fracture mechanism is influenced by the rock fabric, whereas in the shale, tensile type events dominate, the hydraulic fracturing of COS is dominated by shear and compressional events, and only a minor part is of tensile character (Figure SF8). While there are insufficient AE data to generate an accurate hypocenter location, a first motion polarity analysis of the harvested waveforms was able to discriminate AE source types in tensile, shear, and compressional (collapse) type events using the method of Zang et al. (1998; Text S2). Results from the laboratory experiments are consistent with observations from hydraulic fracturing field operations in tight sandstone, where shear type failure events dominated during fracturing (Dusseault, 2013; Warpinski et al., 2004). The shear and compression type events are likely to occur on the fracture flanks as a result of locally increased pore pressures and fluid infiltration, whereas tensile type events are generated at the fracture tip due to the tensile stresses ahead of the fracture tip. Increased pore pressures along the fracture walls aid stick-slip shearing, which generate microseismic AEs (Dusseault, 2013).

5. Conclusions

Using a novel new setup for laboratory (micro)hydraulic fracturing, this study reports a series of experiments on an anisotropic shale and sandstone, and without recourse to a "liner" to impose stress on the inner surface of the borehole. We conclude that hydraulic fracturing in strongly anisotropic mudrocks is governed by its mechanical anisotropy and inherent permeability. For the tight sandstone, this breakdown pressure was not dependent on the inherent anisotropy of the starting material but instead was strongly influenced by the cementation of the rock. We have interpreted our data by dividing the mechanical process into distinct stages of the progressive failure process. These are (i) fracture initiation, (ii) fracture propagation, (iii) breakdown pressure, and (iv) thoroughgoing failure. We conclude that fracture initiation occurs before the physical breakdown of the sample, most likely a consequence of initially stable fracture growth due to a pressure drop within the fracture. The differences in behavior during the final failure phase appear to be controlled by pressure decay, which is in turn driven by the differences in permeability, rock fabric, and anisotropy and fracture geometry. Fracture orientation is primarily controlled by the external stress conditions. Furthermore, the link between the fluid mechanics and the generated AE suggests that induced seismicity could become a powerful tool to define the timing of fracture generation and fracture orientation relative to bedding orientation.

Our experiments allow a connection to be made between key parameters such as fluid injection pressure, seismicity rate, and subsurface deformation (which is normally impossible to measure). Combined, these data have the potential to infer the onset of material breakdown and forecast the onset of a developing fracture network. These links are especially valuable when fractures do not propagate through bedding planes, and where early AE activity indicates breakdown is imminent. We conclude that the anisotropy in mudrocks results in higher breakdown pressures for fracture propagation normal to bedding, as well as higher fluid pressure decay rates and a slower decay process, as well as less deformation of the sample prior to fracture initiation. Finally, we present links between permeability and the anisotropic fabric (including the presence of larger grains) via two conceptual models and show how these fabrics are likely to control fracture characteristics including the pressures required to achieve failure in tension. This is important as such data, when combined with seismic activity, fluid injection rates, and deformation, could be used as indicators for imminent breakdown in anisotropic sedimentary rocks at depth, as well as a monitoring and control tool. Therefore, measurement of these real-world parameters could allow engineers to better apply the tool of hydraulic fracture, allowing resources to be exploited with added safety and efficiency.

Acknowledgments
This work is financed by the National Environmental Research Council (Grant NE/L009110/1). The CT scanning has been performed in the Future Technology Centre at the University of Portsmouth. K. J. D. acknowledges National Environmental Research Council Fellowship NE/M018687/1. The authors thank Emily Butcher for sample preparation assistance and Nathaniel Forbes Inskip for assistance collecting rocks from the field. Data used for this study can be accessed via the U.K. National Geoscience Data Center website (at https://www.bgs.ac.uk/services/NGDC/dataDeposited.html).

References

Aki, K., & Richards, P. G. (1980). *Quantitative seismology: Theory and methods*. San Francisco: Freeman & Co.

Andrews, I. (2013). *The Carboniferous Bowland Shale gas study: Geology and resource estimation*. London, UK: British Geological Survey for Department of Energy and Climate Change.

Atkinson, B. K. (1979). A fracture mechanics study of subcritical tensile cracking of quartz in wet environments. *Pure and Applied Geophysics*, *117*(5), 1011–1024.

Bame, D., & Fehler, M. (1986). Observations of long period earthquakes accompanying hydraulic fracturing. *Geophysical Research Letters*, *13*(2), 149–152.

Benson, P. M., Thompson, B. D., Meredith, P. G., Vinciguerra, S., & Young, R. P. (2007). Imaging slow failure in triaxially deformed Etna basalt using 3D acoustic-emission location and X-ray computed tomography. *Geophysical Research Letters*, *34*, L03303. https://doi.org/10.1029/2006GL028721

Benson, P. M., Vinciguerra, S., Meredith, P. G., & Young, R. P. (2008). Laboratory simulation of volcano seismicity. *Science*, *322*(5899), 249–252.

Benson, P. M., Vinciguerra, S., Meredith, P. G., & Young, R. P. (2010). Spatio-temporal evolution of volcano seismicity: A laboratory study. *Earth and Planetary Science Letters*, *297*(1), 315–323.

Boone, T., Ingraffea, A., & Roegiers, J.-C. (1991). Simulation of hydraulic fracture propagation in poroelastic rock with application to stress measurement techniques. *International Journal of Rock Mechanics and Mining Science and Geomechanics Abstracts*, *28*(1), 1–14.

Burlini, L., Vinciguerra, S., Di Toro, G., De Natale, G., Meredith, P. G., & Burg, J.-P. (2007). Seismicity preceding volcanic eruptions: New experimental insights. *Geology*, *35*(2), 183–186. https://doi.org/10.1130/G23195A.1

Chitrala, Y., Moreno, C., Sondergeld, C. H., Rai, C. S. (2010). Microseismic mapping of laboratory induced hydraulic fractures in anisotropic reservoirs. In: Tight Gas Completions Conference, 2010.

Chouet, B. (2003). Volcano seismology. *Pure and Applied Geophysics*, *160*, 739–788.

Chouet, B. A. (1996). Long-period volcano seismicity: Its source and use in eruption forecasting. *Nature*, *380*(6572), 309–316. https://doi.org/10.1038/380309a0

Clifton, R., Simonson, E., Jones, A., & Green, S. (1976). Determination of the critical-stress-intensity factor K Ic from internally pressurized thick-walled vessels. *Experimental Mechanics*, *16*(6), 233–238.

Collins, D. S., Pettitt, W. S., & Young, R. P. (2002). High-resolution mechanics of a microearthquake sequence. *Pure and Applied Geophysics*, *159*(1– 3), 197–219.

Currie, J., Greenstone, M., & Meckel, K. (2017). Hydraulic fracturing and infant health: New evidence from Pennsylvania. *Science Advances*, *3*(12), e1603021.

Das, I., & Zoback, M. D. (2013). Long-period, long-duration seismic events during hydraulic stimulation of shale and tight-gas reservoirs—Part 1: Waveform characteristics. *Geophysics*, *78*(6), 107–118.

De Pater, H. J. (2015). Hydraulic fracture containment: New insights in to mapped geometry. *Society of Petroleum Engineers*. https://doi.org/10.2118/173359-MS

Detournay, E., & Carbonell, R. (1997). Fracture-mechanics analysis of the breakdown process in minifracture or leakoff test. *SPE Production & Facilities*, *12*(03), 195–199.

Dusseault, M. B. (2013). Geomechanical aspects of shale gas development. In: ISRM International Symposium-EUROCK 2013, 2013.

Eaton, D., van der Baan, M., Tary, J.-B., Birkelo, B., Spriggs, N., Cutten, S., & Pike, K. (2013). Broadband microseismic observations from a Montney hydraulic fracture treatment, northeastern BC, Canada. *CSEG Recorder*, *38*(3), 44–53.

Fazio, M., Benson, P. M., & Vinciguerra, S. (2017). On the generation mechanisms of fluid-driven seismic signals related to volcano-tectonics. *Geophysical Research Letters*, *44*, 734–742. https://doi.org/10.1002/2016GL070919

Ferrazzini, V., Chouet, B., Fehler, M., & Aki, K. (1990). Quantitative analysis of long-period events recorded during hydrofracture experiments at Fenton Hill, New Mexico. *Journal of Geophysical Research*, *95*(B13), 21,871–21,884.

Forbes Inskip, N. D., Meredith, P. G., Chandler, M. R., & Gudmundsson, A. (2018). Fracture properties of Nash Point shale as a function of orientation to bedding. *Journal of Geophysical Research: Solid Earth*, *123*, 8428–8444. https://doi.org/10.1029/2018JB015943

Gandossi, L. (2013). An overview of hydraulic fracturing and other formation stimulation technologies for shale gas production. Eur. Commisison Jt. Res. Cent. Tech. Reports.

Gehne, S., & Benson, P. M. (2017). Permeability and permeability anisotropy in Crab Orchard sandstone: Experimental insights into spatio-temporal effects. *Tectonophysics*, *712*, 589–599.

Gudmundsson, A., & Brenner, S. L. (2001). How hydrofractures become arrested. *Terra Nova*, *13*(6), 456–462. https://doi.org/10.1046/j.1365-3121.2001.00380.x

Haimson, B., & Fairhurst, C. (1969a). Hydraulic fracturing in porous-permeable materials. *Journal of Petroleum Technology*, *21*(07), 811–817.

Haimson, B. & Fairhurst, C. (1969b). In-situ stress determination at great depth by means of hydraulic fracturing. In: The 11th US symposium on rock mechanics (USRMS), 1969.

Harrington, R. M., & Benson, P. M. (2011). Analysis of laboratory simulations of volcanic hybrid earthquakes using empirical Green's functions. *Journal of Geophysical Research*, *116*, B11303. https://doi.org/10.1029/2011JB008373

Hatton, C. G., Main, I. G., & Meredith, P. G. (1994). Non-universal scaling of fracture length and opening displacement. *Nature*, *367*(6459), 160–162. https://doi.org/10.1038/367160a0

He, J., Lin, C., Li, X., & Wan, X. (2016). Experimental investigation of crack extension patterns in hydraulic fracturing with shale, sandstone and granite cores. *Energies*, *9*(12), 1018.

Howell, R. A. (2018). UK public beliefs about fracking and effects of knowledge on beliefs and support: a problem for shale gas policy. *Energy Policy*, *113*, 721–730.

Hurd, O. & Zoback, M. D. (2012). Stimulated shale volume characterization: Multiwell case study from the Horn River Shale: I. Geomechanics and microseismicity. In: SPE Annual Technical Conference and Exhibition, 2012.

Jackson, D., & Mulholland, P. (1993). *Tectonic and stratigraphic aspects of the East Irish Sea Basin and adjacent areas: contrasts in their post-Carboniferous structural styles*, *Petroleum Geology Conference series* (Vol. 4, pp. 791–808). London: Geological Society.

Kumagai, H., & Chouet, B. A. (2000). Acoustic properties of a crack containing magmatic or hydrothermal fluids. *Journal of Geophysical Research*, *105*(B11), 25,493–25,512.

Kumar, A., Hammack, R., Zorn, E., Harbert, W. (2016). Long period, long duration (LPLD) seismicity observed during hydraulic fracturing of the Marcellus Shale in Greene County, Pennsylvania. In: 2016 SEG International Exposition and Annual Meeting, 2016.

Li, N., Shicheng, Z., Zou1, Y., Ma, X., Zhang, Z., Li1, S., et al. (2018). Acoustic emission response of laboratory hydraulic fracturing in layered shale. *Rock Mechanics and Rock Engineering*, *51*, 3395, 11–3406. https://doi.org/10.1007/s00603-018-1547-5

Li, X., Feng, Z., Han, G., Elsworth, D., Marone, C., Saffer, D., & Cheon, D.-S. (2016). Breakdown pressure and fracture surface morphology of hydraulic fracturing in shale with H2 O, CO2 and N2. *Geomechanics and Geophysics for Geo-Energy and Geo-Resources*, *2*(2), 63–76.

Lin, C., He, J., Li, X., Wan, X., & Zheng, B. (2017). An experimental investigation into the effects of the anisotropy of shale on hydraulic fracture propagation. *Rock Mechanics and Rock Engineering*, *50*, 543, 3–554. https://doi.org/10.1007/s00603-016-1136-4

Lockner, D., Byerlee, J., Kuksenko, V., Ponomarev, A., & Sidorin, A. (1991). Quasi-static fault growth and shear fracture energy in granite. *Nature*, *350*, 39–42.

Main, I. G. (2000). A damage mechanics model for power-law creep and earthquake aftershock and foreshock sequences. *Geophysical Journal International*, *142*(1), 151–161. https://doi.org/10.1046/j.1365-246x.2000.00136.x

Martin, C., & Chandler, N. (1994). The progressive fracture of Lac du Bonnet granite. *International Journal of Rock Mechanics and Mining Science and Geomechanics Abstracts*, *31*(6), 643–659.

Mitchell, C., Kurpan, J., Snelling, P. (2013). Detecting long-period long-duration microseismic events during hydraulic fracturing in the Cline Shale Formation, West Texas: A case study. In: 2013 SEG Annual Meeting, 2013.

Montgomery, C. T., & Smith, M. B. (2010). Hydraulic fracturing: History of an enduring technology. *Journal of Petroleum Technology*, *62*(12), 26–40.

Pearson, C. (1981). The relationship between microseismicity and high pore pressures during hydraulic stimulation experiments in low permeability granitic rocks. *Journal of Geophysical Research*, *86*(B9), 7855–7864. https://doi.org/10.1029/JB086iB09p07855

Renard, F., Bernard, D., Desrues, J., & Ougier-Simonin, A. (2009). 3D imaging of fracture propagation using synchrotron X-ray microtomography. *Earth and Planetary Science Letters*, *286*(1), 285–291.

Rubin, A. M. (1993). Tensile fracture of rock at high confining pressure: Implications for dike propagation. *Journal of Geophysical Research*, *98*(B9), 15,919–15,935. https://doi.org/10.1029/93JB01391

Rummel, F., & Hansen, J. (1989). Interpretation of hydrofrac pressure recordings using a simple fracture mechanics simulation model. *International Journal of Rock Mechanics and Mining Science and Geomechanics Abstracts*, *26*(6), 483–488. https://doi.org/10.1016/0148-9062(89)91425-3

Rutter, E. H., & Mecklenburgh, J. (2017). Hydraulic conductivity of bedding-parallel cracks in shale as a function of shear and normal stress. *Geological Society, London, Special Publications*, *454*(1), 67–84.

Sammonds, P. (1999). Understanding the fundemental physics governing the evolution and dynamics of the Earth'crust and ice sheets. *Philosophical Transactions of the Royal Society of London A: Mathematical, Physical and Engineering Sciences*, *357*(1763), 3377–3401.

Schmitt, D., & Zoback, M. (1993). Infiltration effects in the tensile rupture of thin walled cylinders of glass and granite: Implications for the hydraulic fracturing breakdown equation. *International Journal of Rock Mechanics and Mining Sciences & Geomechanics Abstracts*, *30*(3), 289–303.

Schmitt, D. R., & Zoback, M. D. (1989). Poroelastic effects in the determination of the maximum horizontal principal stress in hydraulic fracturing tests – a proposed breakdown equation employing a modified effective stress relation for tensile fracture. *International Journal of Rock Mechanics and Mining Sciences & Geomechanics Abstracts*, *26*(6), 499–506.

Schmitt, D. R., & Zoback, M. D. (1992). Diminished pore pressure in low-porosity crystalline rock under tensional failure: Apparent strengthening by dilatancy. *Journal of Geophysical Research*, *97*(B1), 273–288.

Scholz, C. (1968). Experimental study of the fracturing process in brittle rock. *Journal of Geophysical Research*, *73*(4), 1447–1454.

Sesetty, V., & Ghassemi, A. (2018). Effect of rock anisotropy on wellbore stresses and hydraulic fracture propagation. *International Journal of Rock Mechanics and Mining Sciences*, *112*, 369–384. https://doi.org/10.1016/j.ijrmms.2018.09.005

Stanchits, S., Mayr, S., Shapiro, S., & Dresen, G. (2011). Fracturing of porous rock induced by fluid injection. *Tectonophysics*, *503*(1), 129–145.

Stanchits, S., Surdi, A., Gathogo, P., Edelman, E., & Suarez-Rivera, R. (2014). Onset of hydraulic fracture initiation monitored by acoustic emission and volumetric deformation measurements. *Rock Mechanics and Rock Engineering*, *47*(5), 1521–1532.

Stoeckhert, F., Molenda, M., Brenne, S., & Alber, M. (2015). Fracture propagation in sandstone and slate-Laboratory experiments, acoustic emissions and fracture mechanics. *Journal of Rock Mechanics and Geotechnical Engineering*, *7*(3), 237–249.

Tary, J. B., van der Baan, M., & Eaton, D. W. (2014). Interpretation of resonance frequencies recorded during hydraulic fracturing treatments. *Journal of Geophysical Research: Solid Earth*, *119*, 1295–1315. https://doi.org/10.1002/2013JB010904

Tuffen, H., & Dingwell, D. (2005). Fault textures in volcanic conduits: Evidence for seismic trigger mechanisms during silicic eruptions. *Bulletin of Volcanology*, *67*(4), 370–387. https://doi.org/10.1007/s00445-004-0383-5

Vinciguerra, S., Meredith, P. G., & Hazzard, J. (2004). Experimental and modeling study of fluid pressure-driven fractures in Darley Dale sandstone. *Geophysical Research Letters*, *31*, L09609. https://doi.org/10.1029/2004GL019638

Warpinski, N., Wolhart, S., & Wright, C. (2004). Analysis and prediction of microseismicity induced by hydraulic fracturing. *SPE Journal*, *9*(01), 24–33. https://doi.org/10.2118/87673-PA

Warpinski, N. R., Du, J., & Zimmer, U. (2012). Measurements of hydraulic-fracture-induced seismicity in gas shales. *SPE Production & Operations*, *27*(03), 240–252. https://doi.org/10.2118/151597-PA

Whittaker, B. N., Singh, R. N., & Sun, G. (1992). *Rock fracture mechanics principles, design and applications, developments in geotechnical engineering*. Netherlands: Elsevier Publishers.

Zang, A., Zimmermann, G., Hofmann, H., Stephansson, O., Min, K.-B., & Kim, K.-Y. (2019). How to reduce fluid-injection-induced seismicity. *Rock Mechanics and Rock Engineering*, *52*, 475, 2–493. https://doi.org/10.1007/s00603-018-1467-4

Zang, A., Wagner, F., Stanchits, S., Dresen, G., Andersen, R., & Haidekker, M. (1998). Source analysis of acoustic emission in aue granite cores under symmetric and asymmetric compressive load. *Geophysical Journal International*, *135*(3), 1113–1130. https://doi.org/10.1046/j.1365-246X.1998.00706.x

Zoback, M., Rummel, F., Jung, R., & Raleigh, C. (1977). Laboratory hydraulic fracturing experiments in intact and pre-fractured rock. *International Journal of Rock Mechanics and Mining Science and Geomechanics Abstracts*, *14*(2), 49–58.